High-Frequency Time-Lapse Seismic Spatial Autocorrelation Imaging Shallow Velocity Variations

Fangyu Li, Maria Valero, Yifang Cheng, and WenZhan Song

***Abstract*—Shallow velocity variations can be caused by different reasons, which could be related to infrastructure security. Among seismic-based temporal velocity analysis methods, ambient-noise-based spatial autocorrelation (SPAC) provides the finest shallow imaging resolution. We present a continuous time-lapse SPAC (tSPAC) approach to retrieve the shallow velocity variations. In our field application, due to soil moisture changes caused by water leakage, the seismic velocity changes over the time. Based on the SPAC method, we use the extracted surface wave (Rayleigh wave) to estimate the shear wave velocity as a function of depth. Using a time-lapse manner, we demonstrate that velocity variations due to water leakage can be detected from passive ambient seismic noise. The field deployment results agree well with the ground truth of experiment setups. The success of our study demonstrates that the *in situ* near-surface seismic velocity can be accurately imaged by tSPAC. This technique can be used to monitor seismic velocity change and further investigate not only the fluid saturation, but also other associated changing conditions, such as stress and temperature.**

***Index Terms*—Shallow velocity variation, spatial autocorrelation (SPAC), subsurface imaging, time lapse.**

I. Introduction

INFRASTRUCTURE security is always an important topic. Shallow surface imaging techniques can help characterize the velocity variations caused by soil property changes based on electrical resistivity (ER) tomography [1], [2], ground penetrating radar (GPR) [3], electromagnetic (EM) profile [4], etc. Similarly, near-surface seismic imaging helps monitor shallowly buried objects [5]–[8], for example, very shallow seismic reflection and refraction experiments were conducted to investigate groundwater level changes in beach sand *in situ* [9].

Compared with GPR, ER, and EM methods, seismic-based methods have several advantages, such as low sensor cost, low maintenance, large monitoring area, long period deployment/monitoring capability, and so on. To clearly image temporal evolution of the shallow velocity variation process, we adopt the time-lapse seismic imaging technique, which is widely used in monitoring seismic velocity variations caused by underground mining [10], volcano eruptions [11], oil/gas production at a reservoir [12], reservoir flow [13], CO_2 sequestration [14], major earthquakes [15], and so on. Nowadays, based on seismic ambient noise [16], distributed algorithms [17], and sensor networks [18], [19], continuous time-lapse monitoring becomes easier to implement.

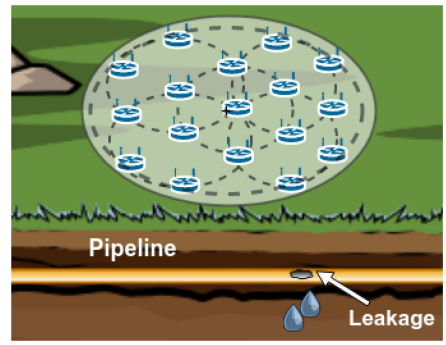

Fig. 1. Time-lapse shallow subsurface imaging can help characterize the infrastructure security, for example, detection of water leakage from shallowly buried pipes.

Compared with the intrusive investigation using borehole survey, passive surface wave methods have gained increasing popularity recently due to their nonintrusive nature [7]. And, there are the increasing number of dense arrays that have been used for imaging the shallowly buried objects recently [20]. The spatial autocorrelation (SPAC) method proposed by Aki [21] and restated in [22] is adopted because of its ability to generate high-resolution images. Moreover, another ambient-noise-based method—seismic interferometry—has also been used to obtain a one-dimensional (1-D) velocity model in Japan [23] and the depth of bedrock in Singapore [6]. Comparing SPAC and seismic interferometry based on their mathematical relationship [24], SPAC is more suitable to be applied to heterogeneous media.

In this article, we propose a time-lapse SPAC (tSPAC) technique to monitor velocity variations, such as water leaks from shallowly buried pipes, as shown in Fig. 1. The passive surface-wave-based approach is attractive because it makes continuous monitoring possible. We conduct field data analysis and show that the proposed method is capable of imaging buried pipes and their surrounding continuous velocity variances. The contributions of this article are as follows.

1) We propose a method (tSPAC) to continuously monitor the velocity changes caused by fluid saturation around shallow infrastructure.

Manuscript received March 11, 2019; revised November 9, 2019; accepted November 14, 2019. Date of publication December 2, 2019; date of current version February 4, 2020. This work was supported in part by the National Science Foundation under Grant 1663709 and in part by Southern Company. *(Corresponding author: Fangyu Li.)*

F. Li, M. Valero, and W. Song are with the Center for Cyber-Physical System, University of Georgia, Athens, GA 30602 USA (e-mail: fangyu.li@uga.edu; maria.valero@uga.edu; wsong@uga.edu).

Y. Cheng is with the Department of Earth Sciences, University of Southern California, Los Angeles, CA 90007 USA (e-mail: chengyif@usc.edu).

Color versions of one or more of the figures in this article are available online at http://ieeexplore.ieee.org.

Digital Object Identifier 10.1109/JSTARS.2019.2954114

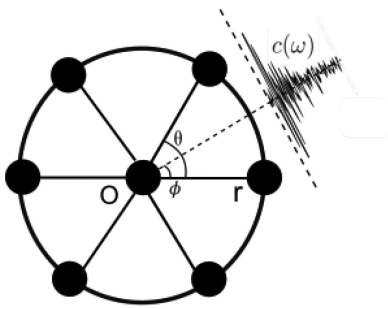

Fig. 2. Plane wave arriving from a single direction ϕ at a given velocity $c(\omega)$.

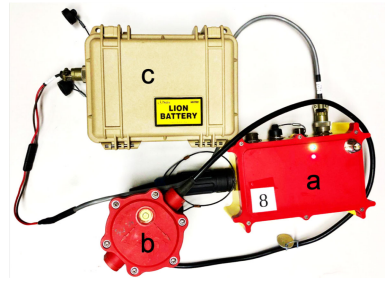

Fig. 3. Prototype instrument, which includes (a) a computation and communication unit, (b) a geophone, and (c) a battery.

2) The proposed algorithm has been implemented with a prototype system. And, we have accomplished a field deployment, where water leakage from a shallowly buried pipeline is clearly imaged.

The remainder of this article is organized as follows. Section II introduces the proposed method. In Section III, we describe the detailed algorithm to implement the proposed method. Our experimental results are presented and discussed in Section IV. Finally, Section V concludes this article.

II. Method

A. SPAC

Aki [21] proposed the SPAC method for surface wave imaging. The normalized azimuthal average coefficient $\bar{\rho}_0(\omega, r)$ is the azimuthal average $\bar{\rho}(\omega, r)$ of the SPAC function $\rho(\omega, r)$ normalized by the central value $\bar{\rho}(\omega, 0)$, expressed as

$$\bar{\rho}_0(\omega, r) = \frac{\bar{\rho}_(\omega, r)}{\bar{\rho}(\omega, 0)} = J_0\left(\omega r / c(\omega)\right) \tag{1}$$

where $J_m(\cdot)$ denotes the Bessel function of the first kind of order m, $c(\omega)$ represents the phase velocity, and ω is the frequency. The propagation of the plane wave through a circular seismic survey is illustrated in Fig. 2.

The SPAC function of a certain period $(0 - \tau)$ between a center point O and the point (r, θ) with distance r and azimuth θ from the point O is defined as the correlation between recorded waveform u at those two points

$$\rho(\omega, r, \theta) = \frac{1}{\tau} \int_0^{\tau} u(\omega, 0, \theta, t) u(\omega, r, \theta, t) dt. \tag{2}$$

Then, the azimuthal average $\bar{\rho}_Z(\omega, r)$ is obtained using the following equation:

$$\bar{\rho}(\omega, r) = \frac{1}{2\pi} \int_{-\pi}^{\pi} \rho_Z(\omega, r, \theta) d\theta. \tag{3}$$

B. Phase Velocity Estimation

Based on (1), the phase velocity $c(\omega)$ can be estimated from the SPAC coefficient ρ. Since a regularly circular array is adopted, the frequency ω is the only variable. Thus, we can use least-squares estimation to solve the phase velocity

$$\min \quad \text{RMS}\left\{\sum^{\omega}\left[\rho(r, \omega_i) - A(\omega_i) J_0\left(\frac{r\omega_i}{c(\omega_i)}\right)\right]\right\} \tag{4}$$

where r is fixed for a given deployment, $A(\omega)$ is a frequency-dependent factor defined in [25], and RMS$\{\cdot\}$ denotes the root-mean-square function. Note that the phase velocity estimation is constrained by the frequency range. As the imaging resolution and sensitive depth range are directly related to the frequency component selection, we can select the specific frequency range to image certain objects at a given depth [26].

C. Time-Lapse Imaging

To achieve the time-lapse imaging, we modify the SPAC function in (2) to a tSPAC version:

$$\rho_{\text{tSPAC}}(t) = \mathcal{T}(\rho_{\text{SPAC}}) = \mathcal{T}\left(\text{SPAC}\left\{u(t)\Big|_{t-\frac{1}{2}\Delta\tau}^{t+\frac{1}{2}\Delta\tau}\right\}\right), t \in \mathbb{R}^+ \tag{5}$$

where $\Delta\tau$ is the analysis window size, $\mathcal{T}(\cdot)$ is an online streaming data processing function, which represents the continuous signal processing, while SPAC$\{\cdot\}$ denotes the SPAC calculation within an analysis window. As an online technique, $\rho_{\text{tSPAC}}(t)$ is calculated and updated using a recorded waveform from the streaming sensor data.

D. Local Normalization

To deal with the issue of unbalanced waveform amplitudes, we design a local normalization operator with a sliding window

$$\bar{u}(t) = \frac{u(t)}{\max\left[|u(t - \Delta\tau/2 : t + \Delta\tau/2)|\right]}. \tag{6}$$

This operator normalizes the recorded data by the maximum absolute value of the correlation in a local window centered around the time t.

III. Algorithm and System Implementation

A. Prototype System

A prototype instrument for implementing the proposed algorithm is shown in Fig. 3, which has a geophone, a global positioning system (GPS), an embedded system, and a battery.

Each sensor node is equipped with a wireless radio to self-form a sensor network for communication and data exchange. The GPS provides the precise time stamp and location information for each node. The main components are inside a waterproof box for protecting them from harsh environment. Our devices were designed and developed to be computation

enabled and energy efficient. Once the battery is connected to the sensors, the system will automatically calibrate itself and find the GPS signal for synchronization. The system parameters are read from configuration files, and the sensor starts working. We implemented the proposed method in a wireless network system. Using a mesh network of seismic but powerful sensors, we use wireless communication and *in situ* computation to generate subsurface velocity images.

B. tSPAC Algorithm

tSPAC can be implemented in a distributed way, which relies on the individual sensors with computation and communication functions. In our system, every node reads data continuously and starts the *in situ signal processing*, including analog-to-digital conversion (ADC), signal segmentation, data compression, transmission over networks, etc. Let $\Delta\tau$ be the analysis window size, which is configurable in the system. Every node individually executes the data preparation, after which the signal is compressed to a suitable size and transmitted in the network to improve the communication cost and meet the bandwidth limitations. We use the *zlib* data compression algorithm [27] and achieve a compression rate of $\sim$50%.

To calculate the correlation between pairs of signals, we transfer the window-prepared signal from each sensor in the survey to the sink sensor[1] of that survey. Notice that this process is performed in parallel for all nodes in the network. In addition, all sensors in the same network are synchronized using GPS to ensure correct data segments are used. We use the user datagram protocol (UDP) for broadcasting the data. When every sink sensor receives the data, it calculates and stacks the correlations according to user needs. For example, the correlation results within 15 min, 30 min, or 1 h can be stacked to improve the signal-to-noise ratio (SNR). Moreover, we can perform the correlations in windows of size $t = 5$ min, and continue doing that for certain hours. The SPAC coefficients are then calculated via (1). Then, the phase velocities are estimated by fitting the observed SPAC coefficients to the Bessel function. Here, the sink sensors are able to calculate a velocity for each frequency (ω). The sink sensors exchange calculated velocity with surrounding sensors through broadcasting, and they perform an interpolation process to form a 3-D map of the subsurface with all the frequencies in consideration. With this information, we can further generate a 4-D velocity model, analyze the velocity variations, and determine and monitor the presence of water leakage. The detailed tSPAC algorithm is shown in Algorithm 1.

IV. Field Application

A. Field Deployment

We deployed the prototype system at Watkinsville, GA, USA, as shown in Fig. 4. Covering the whole target area, there are 13 sensors formulating a circular array as Fig. 2. The target underground pipeline is under the surface at an approximate depth of 0.5 m, as the schematic map shown in Fig. 5.

[1]Sink node is the central node of a distributed sensor network, where all the data collected by other sensor nodes are forwarded to.

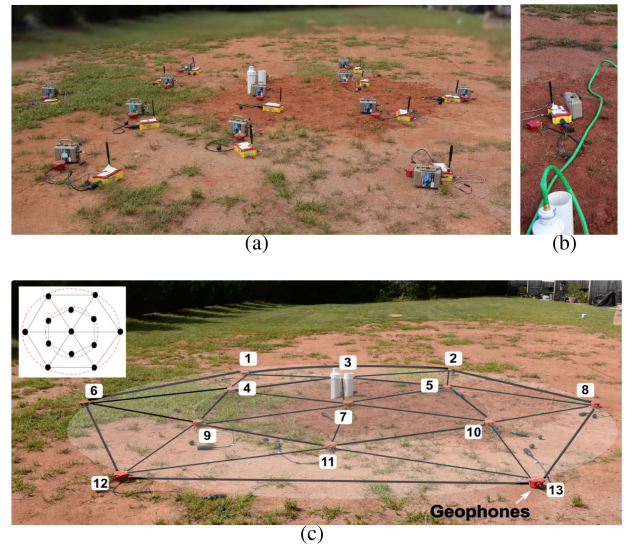

Fig. 4. (a) Deployment location at Watkinsville, GA, USA. (b) Injection of water into the pipeline via a hose. (c) 13 sensors form a circular seismic survey. (The schematic diagram of the geophone array is shown in the upper left corner.) For illustration purposes, we only show the geophones.

Algorithm 1: tSPAC-Based Subsurface Imaging.

Input: Size of analysis window $\Delta\tau$
Input: Station location x_i
While during the deployment period
  Read prepared $u(x_i)$ at position x_i
  for every $\Delta\tau$
    Receive $u(x_j)$ for every j in i ring
    Calculate the pairwise correlation for each j
    Stack correlations for each j
  end for
  Calculate SPAC coefficient $\rho(r, \omega)$ for each ω
  Estimate the phase velocity
  Broadcast phase velocities
  Receive velocities from other k sink sensors
  Interpolate velocity vectors to generate a 3-D velocity model
End While
Output: 4-D velocity model

13 seismic nodes were used for this test, and they formed a seismic mesh network for communication and collaboration. Due to SPAC constraints regarding the distance between sensor nodes, the mesh configuration must be a circular array. Besides, the sensor deployment also considers the geometry of the target object, as shown in Fig. 5. The approximate distance between adjacent sensors was 3 m; they were located over the buried pipeline area. For illustration purposes, we only show the geophone locations (without other instruments) in Fig. 4(c). Note that the instruments should be placed over the infrastructure for the monitoring purpose.

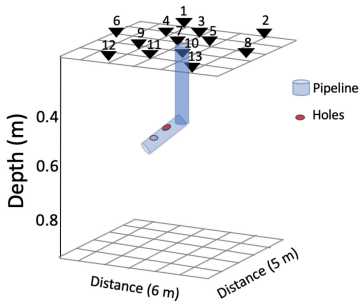

Fig. 5. Schematic map of buried pipeline and the positions of the holes for water leakage.

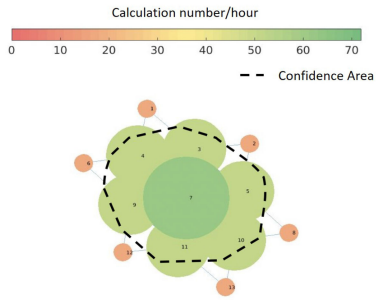

Fig. 7. Confidence map of the SPAC survey.

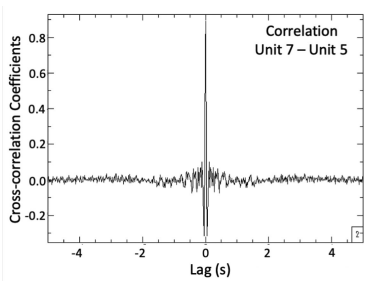

Fig. 6. Symmetric correlation result from nodes 5 and 7 in our deployment.

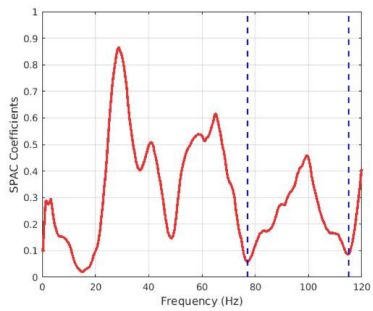

Fig. 8. SPAC coefficient against frequency.

The deployment had three stages: first, we calculated the velocity model of the dry soil without pipe buried; second, after we buried the pipe, the near-surface velocity was calculated; and third, we used the hose on the pipe [as shown in Fig. 4(b)] to inject water; then, the water leaked through the holes. We applied the tSPAC to monitor the velocity variations over the time. The whole deployment lasted for 4 h.

B. SPAC Calculation

Based on (2) and (5), we calculate the correlations between the recorded signals between each node pairs. Each node correlates its signal with its neighboring signals every $\Delta\tau$ time and stacks them together according to the user needs, which enhances the SNR. We configured $\Delta\tau$ to be 5 min, which means that the system correlates every 5 min of data. Fig. 6 shows an example of symmetry correlation we obtain between nodes 5 and 7.

Because of the survey design shown in Fig. 4(c), there are multiple ways to construct correlation pairs. Thus, the correlation calculation density is different for different nodes, resulting in different imaging confidences. We show the number of correlation pairs in Fig. 7. The survey center has the largest correlation density, so the confidence is the highest, and so forth, the boundaries of the survey have lower confidences. According to the largest correlation pair number, we use 80% of the peak pair number as a threshold to circle out a confident area. The dashed line in Fig. 7 is the 80% confidence contour, which is also marked in the following figures.

C. Near-Surface Imaging

Commonly, seismology imaging techniques intend to adopt lower frequencies to map deep structures and avoid spatial aliasing [28]. Lower frequency components penetrate deeper than higher frequency components, while higher frequency components with shorter wavelengths are sensitive to properties of shallower layers [29]. In our study, because of small interstation distances (interval is only 3 m), high-frequency components are available for near-surface imaging.

Fig. 8 shows the SPAC coefficients at different frequencies. Since the surface wave propagates in groups, we can observe that the spectral energies are distributed quite separately. We have compared the velocity maps generated using 1–20, 20–35, 35–50, 50–80, and 80–110 Hz, respectively. In addition, according to the velocity sensitivity kernel theory [30], higher frequencies are needed to image shallow subsurface. We find that the frequency component between ~80 and 110 Hz is the most suitable frequency range to calculate the velocity model via (4). Because different correlation pairs and different time periods could have different velocities, we show not only the final velocity curve, but also the confidence area in Fig. 9.

D. tSPAC-Based Water Leakage Monitoring

Based on the selected frequency range, we can generate continuous near-surface velocity models. Fig. 10(a) shows the initial velocity before we buried the pipe, and Fig. 10(b) shows the velocity model after the pipe was buried but before the water injection. It is clear that before the pipe was buried, the velocity

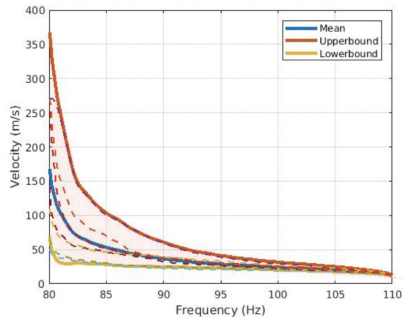

Fig. 9. Velocity estimated from (4) on node 7. The shadow area indicates the possible velocities, and the blue line is the final velocity curve.

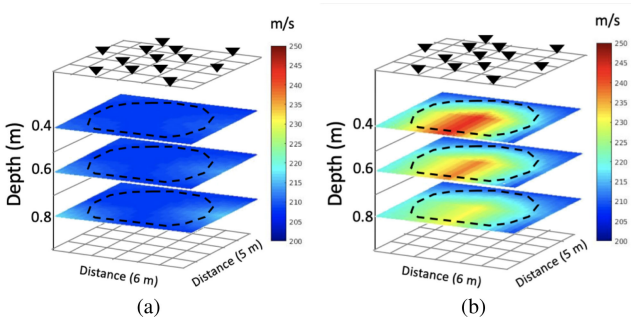

Fig. 10. (a) Velocity structure without pipelines. (b) Velocity structure with buried pipelines.

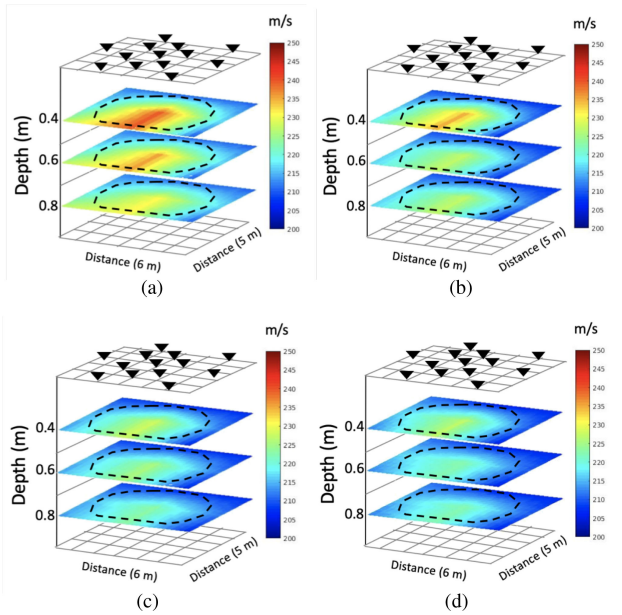

Fig. 11. Velocity structures after (a) 1 h, (b) 2 h, (c) 3 h, and (d) 4 h of water leakage.

is quite uniform in the deployment area; then, the velocity model changes because of the buried pipe.

Fig. 11(a)–(d) displays the time-variant velocity models. Because of the water leakage, the velocity near the pipe location decreases with the time. Notice that, because of the holes shown

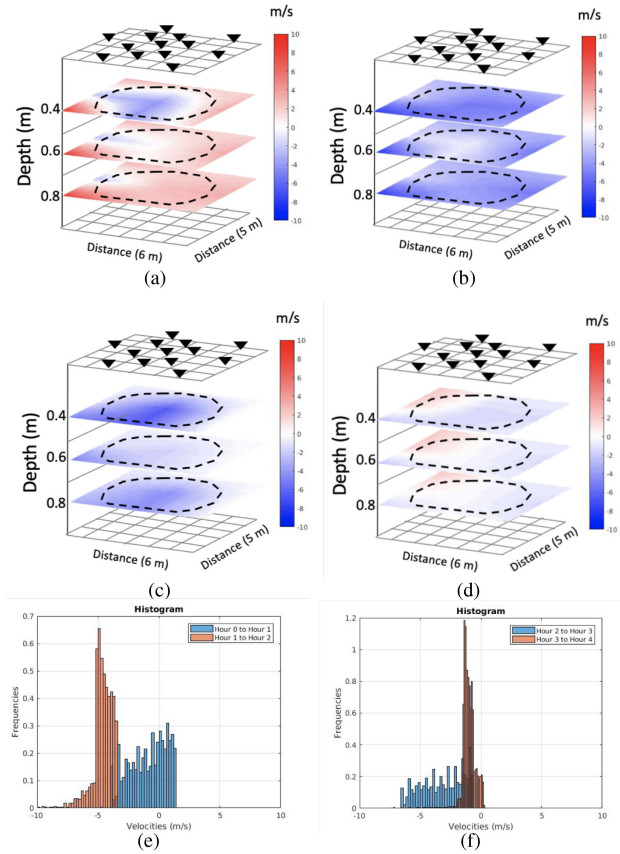

Fig. 12. Velocity variations from (a) 0 to 1 h, (b) 1 to 2 h, (c) 2 to 3 h, and (d) 3 to 4 h. Histogram of velocity variations from (e) 0 to 2 h and (f) 2 to 4 h.

in Fig. 5, the velocity variations are not uniform in all directions and areas.

To further analyze the velocity variation pattern, we show velocity changes in Fig. 12. Notice that the velocity differences were larger between 1 and 3 h than the beginning and the end of the deployment. The histograms in Fig. 12(e) and (f) also validate our observations that the velocity decrease rate is larger between 1 and 3 h than the other time periods. Our interpretation is that at the beginning of water leakage, the water saturation is not high enough to significantly affect the velocity of the whole survey, and in the end, the soil is close to full saturation, and the velocity change is also small. In addition, Fig. 12(a) shows the initial velocity variations in the first hour, and besides the pipeline surroundings, we can find that another velocity decreasing area is perpendicular to the pipe and located at the hole location shown in Fig. 5, which means although the velocity variation over the whole survey in the first hour is small, the water leakage location can be highlighted.

Fig. 13 shows the velocity variations on different nodes. The solid curves belong to the nodes within the confident zone, while the dashed curves show the velocity changes outside the confident zone. As we expected, in the confident zone, the velocity changes follow our understanding, but in the boundary areas, the velocity could vary randomly within a small range or increase because of unknown reasons.

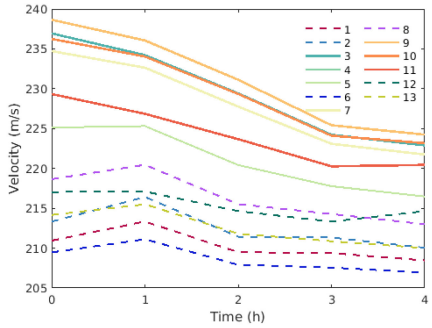

Fig. 13. Velocity changes over the 4-h deployment at different node locations due to the water leakage.

V. Conclusion

The principle of the proposed subsurface imaging was to highlight the velocity variations caused by underground property changes. Based on the seismic ambient noise imaging method, we implemented time-lapse monitoring, and the result clearly showed the velocity change with a high spatiotemporal resolution. Thus, our system was promising for steam/water leakage detection by monitoring its associated seismic velocity change. In addition, the leakage location should be along the pipe system. Combining the imaged pipe and the velocity drop area, we can further infer the leakage location. Furthermore, since the imaging technique is sensitive to the fluid, our system can also be used for watering system monitoring in agriculture via continuously monitoring the water-saturation-triggered soil property variations.

References

[1] A. S. Alamry, M. van der Meijde, M. Noomen, E. A. Addink, R. van Benthem, and S. M. de Jong, "Spatial and temporal monitoring of soil moisture using surface electrical resistivity tomography in mediterranean soils," *Catena*, vol. 157, pp. 388–396, 2017.

[2] T. Jouen, R. Clément, H. Henine, C. Chaumont, B. Vincent, and J. Tournebize, "Evaluation and localization of an artificial drainage network by 3D time-lapse electrical resistivity tomography," *Environ. Sci. Pollut. Res.*, vol. 25, no. 24, pp. 23502–23514, 2018.

[3] S. Demirci, E. Yigit, I. H. Eskidemir, and C. Ozdemir, "Ground penetrating radar imaging of water leaks from buried pipes based on back-projection method," *NDT E Int.*, vol. 47, pp. 35–42, 2012.

[4] Z. He, Z. Hu, Y. Gao, L. He, C. Meng, and L. Yang, "Field test of monitoring gas reservoir development using time-lapse continuous electromagnetic profile method," *Geophysics*, vol. 80, no. 2, pp. WA127–WA134, 2015.

[5] T. Ozdemir, S. Roy, and R. S. Berkowitz, "Imaging of a shallow subsurface objects: An experimental investigation," *IEEE Trans. Geosci. Remote Sens.*, vol. 30, no. 3, pp. 472–481, May 1992.

[6] Y. Zhang, Y. E. Li, H. Zhang, and T. Ku, "Optimized passive seismic interferometry for bedrock detection: A Singapore case study," in *SEG Technical Program Expanded Abstracts 2018*. Tulsa, OK, USA: Society of Exploration Geophysicists, 2018, pp. 2506–2510.

[7] W. Song, F. Li, M. Valero, and L. Zhao, "Toward creating a subsurface camera," *Sensors*, vol. 19, no. 2, 2019, Art. no. 301. [Online]. Available: http://www.mdpi.com/1424-8220/19/2/301

[8] M. Valero, F. Li, S. Wang, F.-C. Lin, and W. Song, "Real-time cooperative analytics for ambient noise tomography in sensor networks," *IEEE Trans. Signal Inf. Process. Netw.*, vol. 5, no. 2, pp. 375–389, Jun. 2019.

[9] R. Bachrach and A. Nur, "High-resolution shallow-seismic experiments in sand—Part I: Water table, fluid flow, and saturation," *Geophysics*, vol. 63, no. 4, pp. 1225–1233, 1998.

[10] R. Czarny *et al.*, "3D S-wave velocity imaging of a subsurface disturbed by mining using ambient seismic noise," *Eng. Geol.*, vol. 251, pp. 115–127, 2019.

[11] X. Zhang and H. Zhang, "Wavelet-based time-dependent travel time tomography method and its application in imaging the Etna volcano in Italy," *J. Geophys. Res., Solid Earth*, vol. 120, no. 10, pp. 7068–7084, 2015.

[12] A. L. Vesnaver *et al.*, "Time-lapse tomography," *Geophysics*, vol. 68, no. 3, pp. 815–823, 2003.

[13] F. Sana, F. Ravanelli, T. Y. Al-Naffouri, and I. Hoteit, "A sparse Bayesian imaging technique for efficient recovery of reservoir channels with time-lapse seismic measurements," *IEEE J. Sel. Topics Appl. Earth Observ. Remote Sens.*, vol. 9, no. 6, pp. 2242–2254, Jun. 2016.

[14] D. Lumley, "4D seismic monitoring of CO_2 sequestration," *Lead. Edge*, vol. 29, no. 2, pp. 150–155, 2010.

[15] I. Koulakov, V. Gladkov, S. El Khrepy, N. Al-Arifi, and I. H. Fathi, "Application of repeated passive source travel time tomography to reveal weak velocity changes related to the 2011 Tohoku-Oki MW 9.0 earthquake," *J. Geophys. Res., Solid Earth*, vol. 121, no. 6, pp. 4408–4426, 2016.

[16] M. Schimmel, E. Stutzmann, and S. Ventosa, "Measuring group velocity in seismic noise correlation studies based on phase coherence and resampling strategies," *IEEE Trans. Geosci. Remote Sens.*, vol. 55, no. 4, pp. 1928–1935, Apr. 2017.

[17] Y. Rizk, H. Partamian, and M. Awad, "Toward real-time seismic feature analysis for bright spot detection: A distributed approach," *IEEE J. Sel. Topics Appl. Earth Observ. Remote Sens.*, vol. 11, no. 1, pp. 322–331, Jan. 2018.

[18] M. Valero, F. Li, J. Clemente, and W. Song, "Distributed and communication-efficient spatial auto-correlation subsurface imaging in sensor networks," *Sensors*, vol. 19, no. 11, 2019, Art. no. 2427.

[19] F. Li, Y. Qin, and W. Song, "Waveform inversion-assisted distributed reverse time migration for microseismic location," *IEEE J. Sel. Topics Appl. Earth Observ. Remote Sens.*, vol. 12, no. 4, pp. 1327–1332, Apr. 2019.

[20] C. Geiss, M. Jilge, T. Lakes, and H. Taubenböck, "Estimation of seismic vulnerability levels of urban structures with multisensor remote sensing," *IEEE J. Sel. Topics Appl. Earth Observ. Remote Sens.*, vol. 9, no. 5, pp. 1913–1936, May 2016.

[21] K. Aki, "Space and time spectra of stationary stochastic waves, with special reference to microtremors," *Bull. Earth. Res. Inst.*, vol. 35, pp. 415–456, 1957.

[22] V. C. Tsai and M. P. Moschetti, "An explicit relationship between time-domain noise correlation and spatial autocorrelation (SPAC) results," *Geophys. J. Int.*, vol. 182, no. 1, pp. 454–460, 2010.

[23] N. Nakata, R. Snieder, T. Tsuji, K. Larner, and T. Matsuoka, "Shear wave imaging from traffic noise using seismic interferometry by cross-coherence," *Geophysics*, vol. 76, no. 6, pp. SA97–SA106, 2011.

[24] H. Nakahara, "Formulation of the spatial autocorrelation (SPAC) method in dissipative media," *Geophys. J. Int.*, vol. 190, no. 3, pp. 1777–1783, 2012.

[25] C. Weemstra, L. Boschi, A. Goertz, and B. Artman, "Seismic attenuation from recordings of ambient noise," *Geophysics*, vol. 78, no. 1, pp. Q1–Q14, 2013.

[26] M. Valero, F. Li, W. Song, and X. Li, "Imaging subsurface civil infrastructure with smart seismic network," in *Proc. IEEE 37th Int. Perform. Comput. Commun. Conf.*, 2018, pp. 1–8.

[27] N. Kimura and S. Latifi, "A survey on data compression in wireless sensor networks," in *Proc. Int. Conf. Inf. Technol., Coding Comput.*, 2005, pp. 8–13.

[28] F.-C. Lin, M. H. Ritzwoller, and R. Snieder, "Eikonal tomography: surface wave tomography by phase front tracking across a regional broadband seismic array," *Geophys. J. Int.*, vol. 177, no. 3, pp. 1091–1110, 2009.

[29] J. Xia, R. D. Miller, C. B. Park, and G. Tian, "Inversion of high frequency surface waves with fundamental and higher modes," *J. Appl. Geophys.*, vol. 52, no. 1, pp. 45–57, 2003.

[30] Y.-Y. Song, J. P. Castagna, R. A. Black, and R. W. Knapp, "Sensitivity of near-surface shear-wave velocity determination from Rayleigh and love waves," in *SEG Technical Program Expanded Abstracts 1989*. Tulsa, OK, USA: Society of Exploration Geophysicists, 1989, pp. 509–512.